

Biomechanical assessment of bicuspid aortic valve phenotypes

Cruz De Oliveira, Diana; Abdullah, Nazirul ; Green, Naomi; Espino, Daniel

DOI:

[10.1007/s13239-020-00469-9](https://doi.org/10.1007/s13239-020-00469-9)

License:

None: All rights reserved

Document Version

Peer reviewed version

Citation for published version (Harvard):

Cruz De Oliveira, D, Abdullah, N, Green, N & Espino, D 2020, 'Biomechanical assessment of bicuspid aortic valve phenotypes: a fluid-structure interaction modelling approach', *Cardiovascular Engineering and Technology*, vol. 11, no. 4, pp. 431-447. <https://doi.org/10.1007/s13239-020-00469-9>

[Link to publication on Research at Birmingham portal](#)

Publisher Rights Statement:

This is a post-peer-review, pre-copyedit version of an article published in Cardiovascular Engineering and Technology. The final authenticated version is available online at: <https://doi.org/10.1007/s13239-020-00469-9>

General rights

Unless a licence is specified above, all rights (including copyright and moral rights) in this document are retained by the authors and/or the copyright holders. The express permission of the copyright holder must be obtained for any use of this material other than for purposes permitted by law.

- Users may freely distribute the URL that is used to identify this publication.
- Users may download and/or print one copy of the publication from the University of Birmingham research portal for the purpose of private study or non-commercial research.
- User may use extracts from the document in line with the concept of 'fair dealing' under the Copyright, Designs and Patents Act 1988 (?)
- Users may not further distribute the material nor use it for the purposes of commercial gain.

Where a licence is displayed above, please note the terms and conditions of the licence govern your use of this document.

When citing, please reference the published version.

Take down policy

While the University of Birmingham exercises care and attention in making items available there are rare occasions when an item has been uploaded in error or has been deemed to be commercially or otherwise sensitive.

If you believe that this is the case for this document, please contact UBIRA@lists.bham.ac.uk providing details and we will remove access to the work immediately and investigate.

1 **Biomechanical Assessment of Bicuspid Aortic Valve Phenotypes: A**
2 **Fluid-Structure Interaction Modelling Approach**

3 Diana M. C. de Oliveira*, Nazirul Abdullah, Naomi C. Green, Daniel M.
4 Espino

5 *Department of Mechanical Engineering, University of Birmingham, Birmingham B15*
6 *2TT, UK*

7 *Diana Marta Cruz de Oliveira; DMC795@student.bham.ac.uk

8

9

10

11

12

13

14

15

16

17

18

19

20

21

22

23 **Acknowledgements**

24 The authors wish to thank ARUP for providing the LS-DYNA and LS-PrePost licenses
25 for version R7.1.2.

26 **Biomechanical Assessment of Bicuspid Aortic Valve Phenotypes: A** 27 **Fluid-Structure Interaction Modelling Approach**

28 Purpose: Bicuspid aortic valve (BAV) is a congenital heart malformation with
29 phenotypic heterogeneity. There is no prior computational study that assesses the
30 haemodynamic and valve mechanics associated with BAV type 2 against a healthy
31 tricuspid aortic valve (TAV) and other BAV categories.

32 Methods: A proof-of-concept study incorporating three-dimensional fluid-
33 structure interaction (FSI) models with idealised geometries (one TAV and six
34 BAVs, namely type 0 with lateral and anterior-posterior orientations, type 1 with
35 R-L, N-R and N-L leaflet fusion and type 2) has been developed. Transient
36 physiological boundary conditions have been applied and simulations were run
37 using an Arbitrary Lagrangian-Eulerian formulation.

38 Results: Our results showed the presence of abnormal haemodynamics in the aorta
39 and abnormal valve mechanics: type 0 BAVs yielded the best haemodynamical
40 and mechanical outcomes, but cusp stress distribution varied with valve orifice
41 orientation, which can be linked to different cusp calcification location onset; type
42 1 BAVs gave rise to similar haemodynamics and valve mechanics, regardless of
43 raphe position, but this position altered the location of abnormal haemodynamic
44 features; finally, type 2 BAV constricted the majority of blood flow, exhibiting the
45 most damaging haemodynamic and mechanical repercussions when compared to
46 other BAV phenotypes.

47 Conclusion: The findings of this proof-of-concept work suggest that there are
48 specific differences across haemodynamics and valve mechanics associated with
49 BAV phenotypes, which may be critical to subsequent processes associated with
50 their pathophysiology processes.

51

52

53 Keywords: bicuspid aortic valve; congenital malformation; fluid-structure
54 interaction; multi-physics modelling

55 **1. Introduction**

56 A bicuspid aortic valve (BAV) is the most common form of congenital heart disease,
57 affecting 1 to 2% of the global population [1]. In a BAV, two cusps are present instead
58 of three (related to a “healthy” tricuspid aortic valve, TAV), being correlated with the
59 onset of valvular pathologies such as aortic stenosis, regurgitation and calcification [2]
60 and with several aortic diseases, such as dissection or dilation [1].

61 A BAV can be categorised as type 0, 1 or 2 [3]. Type 0 is linked to a pure BAV,
62 composed of two distinct cusps. Type 1 has one fusion between two cusps. Given the
63 left, right and non-coronary cusps present in the aortic valve, a BAV type 1 can have
64 fusion between: the right-left (R-L) cusps, non-coronary-right (N-R) cusps and non-
65 coronary-left (N-L) cusps. A BAV type 2, however, has two fusions: R-L and N-L [3].
66 These fusion patterns lead to heterogeneity between BAV phenotypes [3], associated
67 with diverse patterns of flow asymmetry [4-6]. A study evaluating 1362 BAV patients
68 found type 1 to be the most prevalent (79.15 %), followed by type 2 (12.41 %) and then
69 type 0 (8.44 %), reporting similar mortality and morbidity [7]. However, clinical
70 challenges differ: valve regurgitation has been correlated to type 1 R-L BAVs [7], while
71 type 2 BAVs have been associated with the highest incidence of ascending aortic dilation
72 [3, 7]. Further, BAV type 2 may direct valvar flow to the convexity of the ascending
73 aorta, the typical location for onset of dilation (determining whether that increased local
74 wall shear stress acts as a trigger for dilation onset and progress remains challenging)
75 [3].

76 Computational models simulating BAV function have gained interest, as they predict
77 haemodynamic factors not obtainable otherwise [8]. Fluid-structure interaction (FSI)
78 methods have been employed to simulate aortic valve leaflet deformation and blood flow
79 [9-14]. Previous FSI studies have focused either on BAV type 0 [15] or type 1 [16-18]
80 in non-dilated aortas. These studies have used both two-dimensional [15] and three-
81 dimensional [16, 17] idealized models, as well as patient-specific ones [18]. Such models
82 have demonstrated the presence of eccentric and skewed ascending aortic flow,
83 associated with vortices and abnormally high wall shear stress (WSS), when compared
84 to a healthy tricuspid aortic valve (TAV). Other studies have studied the effect of
85 asymmetric BAV models on blood flow [19] and even assessed how different nonfused
86 cup angles in BAV type 1 impact on the valve’s structural and haemodynamic
87 performance [20]. Despite reporting how the wide variation in BAV deformity impacts

88 on aortic blood flow, computational models have not taken into consideration BAV type
89 2, which undergoes an elevated incidence of dilation. It remains difficult to identify
90 common features per BAV phenotype due to elevated clinical variability. However, the
91 assessment of all BAV categories (including type 0, type 1 and type 2) is possible
92 through computational modelling, but such a study has not yet been reported in the
93 literature.

94 The aim of this study is to demonstrate proof-of-concept in developing a standardised
95 platform for simulating and evaluating all BAV types (using the Sievers and Schmidtke
96 categorisation). More specifically type 0 lateral and anterior-posterior, type 1 R-L, N-R
97 and N-L and type 2, as well as a healthy TAV, are compared through a transient systolic
98 FSI model. The objectives within this aim are to analyse the effect of BAV type 0 orifice
99 orientation on aortic haemodynamics and valve mechanics; to determine whether raphe
100 location in type 1 BAVs plays a significant role on blood flow, wall shear stress and
101 valve stress; and to simulate for the first time a BAV type 2 model and assess its
102 haemodynamic and valve mechanics.

103 **2. Methods**

104 ***2.1 Model geometries and grid settings***

105 All models were generated using Solidworks 2013 (Dassault Systemes, Waltham, MA,
106 USA). These consisted of idealised TAV and 6 BAVs with a constant thickness of 0.2
107 mm [9] representing: type 0 with lateral and anterior-posterior orientations, type 1 with
108 R-L, N-R and N-L leaflet fusion and type 2. Cusps in BAVs type 1 and 2 were merged
109 in the free edge, to represent the presence of a raphe (Figure 1). Dimensions employed
110 for all models are presented in Table 1 and displayed in Figure 2, based on clinical
111 measurements [21], consistent with other aortic valve studies [22], and previous BAV
112 models [9, 15, 23]. As per previous studies [24, 25], the geometry of interest was the
113 thoracic aorta, including aortic root, ascending aorta and aortic arch, with the model
114 subsequently truncated at the descending aorta (Figure 3). The same diameter was
115 assumed for ascending and descending aortas. As this study focused on flow at the aortic
116 root and ascending aorta, aortic arch branches were neglected; their exclusion is not
117 expected to alter flow profiles in the regions of interest as a previous FSI study which
118 also excluded supra-aortic branches [26] predicted flow, such as peak flow velocities,
119 consistent with clinical observations [27, 28].

120 [Table 1 near here]

121 [Figure 1 near here]

122 [Figure 2 near here]

123 [Figure 3 near here]

124

125 All geometries were meshed using ANSYS (Ansys Inc., Canonsburg, PA, USA) and one
126 example is provided in Figure 3 a). Aortic models were based on a previously published
127 study, which included mesh convergence analysis [23]; however, in FSI, the fluid ALE
128 mesh shape conforms to the structural mesh, and fluid-solid mesh nodes are shared at
129 the interface, meaning that any mesh refinement for one of the meshes results in a
130 refinement of the mesh for the other domain at their interface. This may lead to a non-
131 homogeneous mesh with implications for computational cost [29]. Therefore, mesh
132 quality measures were the primary choice for model mesh assessment [30]. 20,900
133 hexahedral elements were created for the aortic model (fluid domain) to reduce
134 computational time, while the valve leaflets (structural domain) were meshed with 5700
135 quadrilateral and triangular shell elements. The Belytschko-Lin-Tsay shell element
136 formulation was employed to increase computational efficiency [31]. To avoid stepping
137 artefacts in WSS which can occur with mesh refinement at boundary walls, no additional
138 mesh refinement was added. A spatial resolution of 0.87 mm and 2.5 mm was then
139 achieved for the structural and fluid meshes, respectively. Mesh quality was assessed
140 through element skewness and orthogonal quality, which yielded average values of
141 0.2255 and 0.8832. According to quality criteria, the meshes had excellent skewness
142 (between 0 and 0.25) and very good orthogonal quality (between 0.70 and 0.95) [30, 32].

143 ***2.2 Material properties and boundary conditions***

144 Blood flow was approximated as a Newtonian and virtually incompressible fluid, a valid
145 assumption for large scale flow in the cardiovascular system [33]. This material model
146 was used in conjunction with the Grüneisen equation of state, which describes how
147 volumetric changes affect the fluid reference pressure [32, 34]. The Grüneisen equation
148 can be defined as:

$$p = \frac{\rho_0 C^2 \mu \left[1 + \left(1 - \frac{\gamma_0}{2} \right) \mu - \frac{a}{2} \mu^2 \right]}{\left[1 - (S_1 - 1) \mu - S_2 \frac{\mu^2}{\mu + 1} - S_3 \frac{\mu^3}{(\mu + 1)^2} \right]^2} + (\gamma_0 + a \mu) E, \quad (1)$$

149

150 where ρ_0 is the initial fluid density (1000 kg/m³); C is the elastic sound speed (set as
151 1500 m/s to increase blood's bulk modulus and make it a virtually incompressible fluid
152 [35]); γ_0 is the Grüneisen parameter (1.65); a is the first order volume correction to γ_0
153 (0); S_1 , S_2 and S_3 are equation coefficients (1.79, 0, 0); E is the fluid initial internal
154 energy (0 J). Blood flow compression is defined in terms of a relative volume V as:

$$\mu = \frac{1}{V} - 1 = \frac{\rho}{\rho_0} - 1, \quad (2)$$

155

156 where ρ is the blood density.

157

158 Linear elastic material properties were assigned to the aortic valve tissue, based on the
159 reported range of cardiac tissue deformation [36-38] and previous studies [9, 15, 22, 39,
160 40]. The Young's modulus has been chosen to mimic valve behaviour as closely as
161 possible. A density of 1000 kg/m⁻³, a Poisson's ratio of 0.49 and a Young's modulus of
162 1.5 MPa were employed, based on a previous computational study [15]. The density of
163 blood was set equal to that of the aortic valve to negate the effects of buoyancy, and its
164 dynamic viscosity was assumed to be 4.3 mPa s [32, 33].

165 Time-dependent physiological flow conditions were applied at the aortic inlet and outlet
166 (specified in Figure 3), with the inflow profile representing left ventricular ejection
167 (Figure 4). These were modelled with spatially uniform velocity profiles. A fluid
168 reference pressure of 80 mmHg was employed to simulate initial (diastolic) blood
169 pressure. The aortic wall boundaries were assumed rigid and a no-slip condition was
170 employed at the wall-blood interface. The same assumption was made for the TAV
171 model, enabling like-for-like comparisons across BAV models. Similarly, a no-slip
172 condition was enforced between the cusps and blood flow. Valve cusp edges were also
173 fixed to constrain their movement within the aortic root.

174

175 [Figure 4 near here]

176 ***2.3 Fluid-structure interaction framework and study settings***

177 The finite element software LS-DYNA 4.5.12 (LSTC, Livermore CA, USA) was used
178 to implement and solve the FSI between blood flow and aortic valve cusp deformation.
179 This software has been used previously for modelling aortic valve movement [22, 39-
180 41]. An Arbitrary Lagrangian-Eulerian (ALE) formulation was chosen, where fluid

181 dynamics were solved using the continuity and incompressible Navier-Stokes equations
182 (discretization of the fluid domain into solid LS-DYNA ALE fluid elements) and
183 structural deformation using the linear elastic equation for isotropic, linear and elastic
184 materials [42, 43]. Fluid flow was coupled to the valve structure by a penalty coupling
185 method [32], similar to previous studies [22, 40, 41]. An hourglass control was also
186 applied to prevent zero strain energy. The transient study was solved using the explicit
187 hydrodynamic solver available in LS-DYNA and free-time stepping up to a total time of
188 0.8 s. Focus was given to the systolic phase of the cardiac cycle (referred to in the rest
189 of this paper as 0 – 0.4 s), with results being obtained for this time period. All numerical
190 simulations were performed on an Intel i7-9700 CPU with 16GB of DDR4 RAM
191 workstation and took approximately > 30 hours to solve.

192 **2.4 Mechanical and haemodynamic characterisations**

193 Data post-processing was performed with LS-PrePost and MATLAB (R2017b v. 9.3.0,
194 MathWorks, Natick, MA, USA). Von Mises stress was assessed at the valve cusps, while
195 global aortic haemodynamics are reported for peak systole (time, $t = 0.125$ s) focusing
196 on flow velocity, vortices, and pressure. Three cross-section planes were created for
197 further haemodynamic quantification (planes B-B, C-C and D-D from Figure 3c.), their
198 position similar to cross-sectional planes employed for 4D magnetic resonance imaging
199 (MRI) measurements used *in vivo* [44].

200 Peak systolic transvalvular pressure across the aortic valve was obtained by calculating
201 the averaged pressure before and after the valve (Equation 3),

$$\Delta P = P_u - P_d, \quad (3)$$

202

203 where P_u is the upstream pressure (aortic inlet boundary) and P_d is the downstream
204 pressure (B-B cross-section).

205 Systolic retrograde flow was quantified at the cross-section B-B using MATLAB and
206 through the systolic flow reversal ratio (FRR; Equation 4) index [45, 46],

$$\text{FRR} = \frac{|Q_n|}{|Q_p|} \%, \quad (4)$$

207

208 where Q_n and Q_p are the backward and forward flow rates at the cross-section of interest,
 209 respectively (when FRR equals 0, no retrograde flow is present). Surface integrals were
 210 defined for each element to determine the associated flow rate, as given by

$$Q = \int_{\Gamma} \mathbf{t}(t) \cdot \mathbf{n} \, d\sigma, \quad (5)$$

211
 212 where Γ is the finite element area of interest, t is the time instant, \mathbf{n} is the normal plane
 213 vector and σ is the finite element area limit, respectively.

214 The geometric (GOA) and effective (EOA) orifice areas were also calculated. The GOA
 215 was obtained by finding the planar area of each aortic valve orifice at peak systole. The
 216 EOA was calculated using a modified version of the Gorlin equation, written as:

$$EOA = \frac{Q_{rms}}{51.6\sqrt{\Delta P}}, \quad (6)$$

217
 218 where Q_{rms} is the root mean square systolic flow rate (cm^3/s), ΔP is in mmHg and EOA
 219 is in cm^2 [47].

220 MATLAB was used to quantify WSS magnitudes at the defined cross-sections using
 221 equation 7,

$$WSS = \mu \frac{\mathbf{v} \cdot \mathbf{n}}{y}, \quad (7)$$

222
 223 where μ represents the dynamic viscosity of the fluid, \mathbf{v} is the velocity vector and y is
 224 the perpendicular distance between each velocity vector and the aortic wall [44].

225 **3. Results**

226 ***3.1 Blood Haemodynamics***

227 Peak velocity, transvalvular pressure drop, FRR and GOA and EOA results are presented
 228 in Table 2, listed along with published values for comparison.

229 ***3.1.1 Blood flow velocity and asymmetry***

230 BAV models generated higher peak velocity magnitudes (> 2.2 m/s) in comparison with
 231 the TAV model (1.52 m/s). Among all BAVs, type 2 yielded the highest peak velocity
 232 value (3.7 m/s), while type 0 lateral generated the lowest (2.2 m/s), corresponding to a

233 150% and 38% increase when compared with the TAV, respectively. Type 1 BAVs
234 predicted similar peak velocity magnitudes, regardless of raphe position.

235 While TAV generates a symmetrical and dispersed flow profile, BAV models give rise
236 to an asymmetric distribution of the velocity field (Figure 5 and Supplementary Figure
237 S1), characterized by the presence of concentrated high velocity flow. Flow direction
238 varies according to the type of BAV; while elevated blood velocities are present at the
239 centre of the ascending aorta in type 0, type 1 yields peripheral skewing of the systolic
240 jet towards the aortic wall: BAVs R-L, N-R and N-L direct the jet towards the right-
241 anterior, posterior and anterior portions of the ascending aortic wall, respectively. BAV
242 type 2, instead, outputted the lowest flow volume of elevated peak systolic velocity in
243 comparison with the remaining BAVs, associated with a greater flow constriction.

244

245 [Figure 5 near here]

246 [Table 2 near here]

247

248 The TAV generated mainly unidirectional flow in the ascending aorta, with the presence
249 of small low velocity vortices (Figure 6). In all BAV cases, there was the development
250 of stronger vortices with greater velocity in comparison with the healthy valve.
251 Asymmetric flow is showed for type 0 and type 1 BAVs with the generation of counter-
252 rotating vortices. Vortex spatial distribution was influenced by valve orifice location and
253 the position of the raphe in type 1 BAVs, with two major vortices developing above the
254 fused cusps. In BAV type 2, high velocity flow was directed towards the aortic wall,
255 accelerating in opposite directions.

256

257 [Figure 6 near here]

258 *3.1.2 Retrograde flow*

259 Systolic retrograde flow was present in the ascending aorta in all BAV models (> 3.5%),
260 contrasting with the TAV (0%), as given by the FRR index (Table 2). The lowest FRR
261 was predicted for type 0 lateral (3.5%), while type 2 yielded the highest FRR (13.3%).
262 However, the presence of a raphe in type 1 BAVs gave rise to a higher generation of
263 retrograde flow in comparison with the pure BAVs. Nonetheless, FRR values were
264 similar among type 1 sub-phenotypes.

265 *3.1.3 GOA and EOA*

266 A reduction in GOA and EOA was observed for all BAVs in comparison with the
267 tricuspid valve. According to clinical guidelines, the EOA for TAV is considered normal
268 (3 - 4 cm²), while type 0 and 1 BAVs yielded EOAs which are considered mildly stenotic
269 (1.5 – 2 cm²). While type 0 BAVs yielded the same EOA, type 1 BAVs were associated
270 with higher EOA values, with the R-L phenotype having the lowest orifice area. BAV
271 type 2 had the greatest reduction in EOA, corresponding to a moderate stenosis range (1
272 – 1.5 cm²).

273 *3.1.4 Transvalvular pressure drop*

274 The peak transvalvular pressure gradients predicted by the BAV models were greater
275 than the one predicted by the TAV (4.5 mmHg). Among all BAV phenotypes, type 2
276 BAV gave rise to the greatest pressure drop (37 mmHg), with an increase of more than
277 700% from the pressure gradient obtained for the TAV. Both type 0 BAVs yielded the
278 same transvalvular pressure drop (15 mmHg) and among type 1, the R-L phenotype was
279 associated with the highest pressure drop (15 mmHg).

280 *3.2 Characterisation of stresses*

281 Peak systolic WSS (at the B-B cross section) and valve cusp Von Mises stress are listed
282 in Table 3, along with published values. TAWSS and OSI have also been computed and
283 made available in the Supplementary Figures S2 and S3. To avoid repetition in the
284 analysis commentary, the main text in the sections below is focused on time-dependent
285 results.

286

287 [Table 3 near here]

288

289 *3.2.1 Wall shear stress*

290 Peak systolic WSS magnitudes are displayed in Figure 7 for all models, across the
291 ascending aorta. Type 0 BAVs yielded low WSS magnitudes; however, all other BAV
292 models yielded greater WSS magnitudes in comparison with the TAV. The presence of
293 a raphe in type 1 BAVs gave rise to higher WSS magnitudes in comparison with the pure
294 BAVs, due to the eccentricity associated with the systolic flow jet and its direction
295 towards the ascending aortic wall. The highest WSS magnitude was predicted for type 2

296 BAV (5.08 Pa), which is 10 times higher than the lowest WSS value for type 0 BAV.
297 Type 1 and 2 BAVs gave rise to progressively decreasing WSS values along the
298 ascending aorta, from the sinotubular junction (B-B section) to the distal regions (D-D
299 section). Also, WSS magnitudes did not greatly vary within each BAV phenotype: type
300 0 BAVs generated similar WSS values along the ascending aorta and in type 1 BAVs,
301 the WSS magnitudes corresponded to a standard deviation of only ± 0.2 Pa, showing that
302 the position of the raphe does not greatly influence this magnitude amongst sub-
303 phenotype categories.

304

305 [Figure 7 near here]

306

307 3.2.2 Cusps stress

308 Type 2 BAVs presented with the highest peak Von Mises stress (1.6 MPa - Table 4),
309 almost 500% greater than the lowest BAV peak stress (BAV type 0 anterior-posterior;
310 0.27 MPa). Peak systolic Von Mises stress values were similar among type 1 BAVs.
311 Increases in the area-averaged Von Mises stress from BAV models, in comparison with
312 the TAV are displayed in Figure 8, focusing on the systolic acceleration phase and
313 systolic peak. Although BAV type 0 anterior-posterior had a lower peak stress than
314 TAV, its area-averaged stress was greater for the phases mentioned above. This is due
315 to how the stresses are distributed across the cusp surfaces (Figure 9). Here, while the
316 TAV model was associated with lower and more evenly distributed stresses, the BAV
317 models displayed elevated and concentrated stresses at the constricted edges, more
318 evident for BAVs type 1 and 2. Concerning type 0 BAVs, the valve orifice orientation
319 influenced peak stress distributions on the cusps: while the lateral phenotype had more
320 concentrated stress at the constricted edges adjacent to the orifice, such a feature was not
321 present for the anterior-posterior configuration. Despite this, both phenotypes presented
322 with marks of elevated stress at the middle of both cusp bellies. Type 1 BAVs presented
323 with identical cusp stress distributions among one another, with concentrated stresses
324 located at the raphe; nonetheless, phenotypes N-L and N-R also had high stresses at the
325 belly of the non-fused cusp, adjacent to the valve orifice, coincident with the direction
326 of the systolic flow jet for each case represented in Figure 5. This was not present,
327 however, on phenotype R-L. Higher contour stresses were observed all over the cusps
328 for BAV type 2, with the greatest stress located at the raphes near the valve orifice.

329

330 [Figure 8 near here]

331 [Figure 9 near here]

332 4. Discussion

333 4.1 Main study findings

334 FSI has been used to simulate congenitally malformed aortic valves. Type 0, 1 and 2
335 BAVs were simulated, including sub-classifications, and referenced against a TAV
336 model. This approach enabled the first and object comparison of the key features of BAV
337 type 2 against other BAV types and subcategories, as regards subsequent flow and
338 stresses induced; only possible using idealised models. The obtained results suggest the
339 following findings:

- 340 • The TAV model haemodynamic and mechanical predictions are consistent with
341 those available *in vivo* [4, 6, 44, 48], *in vitro* [49, 50] and *in silico* [16, 17, 23,
342 46, 51] literature, therefore, validating our computational model;
- 343 • All BAV phenotypes induce abnormal haemodynamics in the aorta when
344 compared to the TAV model;
- 345 • Concerning BAV phenotypes, type 0 has the lowest peak velocity magnitude,
346 FRR, WSS magnitude and cusp stress, presumably leading to the least impact
347 out of all types. The orientation of the valve in BAV type 0 influences the stress
348 on the cusps in terms of maximum magnitude reached and its location, but global
349 haemodynamic quantifications are not sensitive to its orientation. Regions of
350 high and low WSS on the aorta, however, are determined by the orientation of
351 the BAV type 0;
- 352 • The raphe location in type 1 BAVs influences the spatial distribution of
353 haemodynamic features; nonetheless, these yield similar haemodynamic
354 magnitudes (velocity and WSS) and valve stress values, regardless of the
355 location of raphe.
- 356 • BAV type 2 exhibits the highest values in haemodynamic parameters (peak
357 velocity, pressure gradient and FRR) and lowest GOA and EOA, as well as
358 highest valve stresses, presumably leading to the most damaging repercussions
359 when compared to other BAV phenotypes.

360 **4.2 Computational model validation and design framework**

361 In this study, idealised geometries were used for the aorta and the aortic valve based
362 upon clinical data and previous computational studies [9, 15, 21]. In reality, both
363 geometric and functional factors related to aortic valve function are heterogeneous and
364 no two patients present with the same morphological characteristics in a BAV population
365 [52]. However, idealised computational modelling enables an unbiased comparison
366 amongst BAV models not feasible clinically, such as the influence of valve orifice
367 orientation on blood jet direction or the impact of the presence of a raphe in the overall
368 cusp mechanics and haemodynamics.

369 All results for the healthy TAV model were in agreement with clinical measurements, *in*
370 *vitro* experiments, and previous computational models: peak systolic velocity
371 magnitudes differed by less than 35% and 20% when compared to other three-
372 dimensional FSI models [16] and 4D MRI measurements [4-6], respectively. Indeed,
373 some of this quantitative discrepancy would be accounted for by the specific differences
374 in the models solved; qualitatively, all TAV model predictions were consistent with
375 literature. For example, flow patterns with the development of small low velocity
376 vortices were comparable to computational results presented elsewhere [53, 54].

377 Comparison of our TAV predictions with *in vivo* measurements was considered
378 primordial and *in vitro/in silico* results were second choices of validation, due to the fact
379 that any obtained data is subject to individual experimental bias or computational
380 assumptions. Previous computational studies have used WSS magnitudes as a measure
381 of the stress on the aortic valve cusps [55, 56]; however, this measure of stress only takes
382 into account parallel forces acting on the valve surface. Thus, the Von Mises criterion
383 was used as a measure of valve stress. WSS and Von Mises values predicted were
384 consistent with previous computational studies modelling the TAV [16, 17, 51, 57].

385 **4.3 Clinical impact of abnormal BAV haemodynamic and mechanical features**

386 The BAV models were associated with lower GOA and EOA values, in comparison with
387 the normal TAV, something which is expected to increase peak velocity and ΔP . Indeed,
388 our models predicted an increase in most of the haemodynamic parameters studied,
389 including peak systolic velocities, ΔP , FRR and WSS, as well as higher peak and average
390 Von Mises stress on the valve cusps. These results further support the already well

391 established awareness that BAV is associated with abnormal ascending aortic
392 haemodynamics [6, 16, 49].

393 The FRR predicted by type 0 BAV was much lower than the literature reports [46];
394 however, values in our study were derived from an FSI study whereas Bonomi et al.
395 (2015) used CFD, with cusps in a single, fixed configuration.

396 The TAV ΔP value was consistent with the literature, while the values obtained for type
397 0 BAVs were 30% lower than previous *in silico* results (Table 2). Nonetheless, the
398 reduced valve systolic orifice associated with our BAVs yielded consistently greater ΔP
399 than the TAV, in agreement with the literature [58]. According to the obtained EOA,
400 their configuration is considered mildly (types 0 and 1) or moderately (type 2) stenotic
401 [59-61], even without cusp calcification or stiffening, which can overload left ventricular
402 pressure with the potential for subsequent heart failure [62]. Moreover, all BAV models
403 had elevated Von Mises stresses, which are associated with denudation of cusp
404 endothelial cells, potentially leaving the valve susceptible to bacterial infections [63].
405 This information is relevant, because BAV patients have a greater propensity for
406 infections. In addition, predicted cusp stresses increased with lower EOA, with BAV
407 type 2 presenting with the highest stresses of all phenotypes. This suggests that type 2
408 BAV patients may be at greater risk of valve degeneration, which could result in severe
409 aortic stenosis, heart tissue damage and myocardial infarction [64].

410 ***4.4 Different BAV phenotypes impact differently on aortic haemodynamics and*** 411 ***mechanics***

412 Previous computational studies have suggested that the elevated stresses present in BAV
413 cusps can be associated with calcification development, leading to stiffer cusps,
414 contributing to the obstruction of the left ventricular outflow [54, 65], as well as valve
415 stenosis and aortic regurgitation [2]. Moreover, Conti et al. (2010) have noted increased
416 stress at the belly region of a type 0 BAV model. Thus, and as per their results, the
417 location of calcification onset may be sensitive to type 0 BAV orientation, due to the
418 presence of peak stresses in different regions. Nonetheless, our type 0 BAVs presented
419 with the lowest peak velocity and WSS magnitudes, FRR and Von Mises stress values,
420 suggesting that, from all BAV phenotypes, this is likely the subtype with the least clinical
421 impact.

422 Although Type 1 BAVs yielded different jet orientations with counter-rotating vortices,
423 generating diverse spatial regions of elevated velocity (Figure 5), results suggest that
424 raphe location does not have a great impact on blood peak velocity and WSS magnitudes
425 and cusp stress, consistent with findings from Cao et al. (2017). However, these peak
426 velocities were higher than the ones predicted for the TAV, also associated with
427 increased average WSS in the ascending aorta. WSS is an important vascular regulator
428 that can induce vascular remodelling by directly influencing endothelial cell function
429 [66]. This then contributes towards aortic wall degeneration, associated with aortic
430 dissection [67] and dilation [67, 68] and present in BAV patients [69]. Therefore,
431 increased WSS in the ascending aorta may anticipate the onset of aortopathy and
432 contribute to its triggering [24]; which is consistent with our present results that suggest
433 increases in the average WSS along the ascending wall of aorta (measured at three
434 distinct cross-sections along the wall of the ascending aorta). Clearly, this is an area
435 which merits further investigation.

436 Type 2 BAV yielded what is presumed to be the most compromised haemodynamic and
437 mechanical characteristics among all BAV phenotypes, including the highest peak
438 systolic velocity and WSS magnitudes. It is hypothesised that BAV patients with
439 worsened aortic stenosis might be at greater risk for aortic dilation onset and progression
440 [70] and this may afflict individuals with a type 2 BAV in particular. Such a hypothesis
441 is consistent with the current literature [3, 7] but clearly needs to be tested.

442 ***4.5 Clinical applications***

443 The results obtained in this study show the importance of BAV patient stratification
444 according to categories, since specific phenotypes differ in hemodynamic (peak velocity,
445 FRR and pressure gradient) and mechanical measures (Von Mises stress, WSS). The use
446 of indicators such as WSS may be useful to estimate the risk of dilation in BAV patients,
447 by estimating phenotypes with a larger risk for dilation onset and progression. Aortic
448 wall mechanics for BAV patients is fundamentally different than for TAV patients: BAV
449 patients present with ascending aortic wall structural changes resulting in excessive
450 stiffness and reduced compliance in comparison with patients with a normal TAV [71,
451 72]. In fact, a previous study reported a 109.8% increase in the aortic wall stiffness index
452 for BAV patients in comparison with TAV ones [73]. However, these studies refer to
453 the BAV population, not differentiating across phenotypes. Therefore, since the

454 available information on ascending aortic wall properties for BAV patients (and different
455 phenotypes) is limited, the use of WSS to predict the possibility of damage to the aortic
456 wall in specific categories, as well as regions of potential damage, can prove useful. This
457 can be especially important for BAV type 2 patients, which have been computationally
458 simulated here for the first time and have presented with presumably the most
459 compromised mechanical and hemodynamic changes.

460 **4.6 Limitations**

461 Several limitations were present in this study. First, our aortic model presents with an
462 in-plane curvature for the ascending portion, while a physiological aorta has typically an
463 out-of-plane curvature. However, previous studies report that ascending aortic curvature
464 can be seen as an independent risk factor for wall dissection or dilation onset [74], where
465 a greater curvature is associated with worsened outcomes [75]. Since here we were
466 focused on the comparison between BAV models, we chose an in-plane curvature aortic
467 model.

468 Time-independency of the predictions was not assessed in this study; nonetheless, while
469 parameters may reach convergence over a couple of cycles, any bias from such changes
470 is expected to be consistent across the difference BAV phenotypes simulated. Further,
471 we used direct validation against data available in literature to assess the accuracy of our
472 models. Although only one systolic phase was modelled, consistent with a previous
473 study [22], the same comparison was performed for all models, and so any trends are
474 expected to be consistent across the simulations performed, not altering the ultimate
475 conclusions from this proof-of-concept study.

476 In this study, blood flow was assumed to be laminar. In reality, the Reynolds number in
477 the ascending aorta can reach values between 3000 and 3900 at peak systole, owing to
478 the aortic valve opening and closure and the geometry of the aorta itself [76]. In BAV
479 patients, the abnormal shape of the valve can lead to transitional blood flow, which might
480 approach turbulent flow [77]. This is more likely the case for stenotic valves (such as the
481 type 2 BAV). However, appropriate turbulence models for aortic flow have been
482 identified as a current challenge [70, 77, 78], and may not be suitable for FSI problems
483 [55, 79]. Critically, turbulence models may lead to very different predictions for WSS in
484 healthy aortas which would likely not be appropriate for comparison to laminar flow
485 models; for example, comparison of WSS and velocity for laminar and turbulence

486 models in an aortic aneurysm led to predictions which different by a factor of around $\times 2$
487 (data in supplementary material: [80]). In addition, a previous study employing laminar
488 flow to study aortic valve calcification did not find a laminar flow model to limit the
489 predicted results [26]. With such studies in mind, we do not view the use of a laminar
490 model as leading to fewer limitations than the use of a turbulence model.

491 In this study, the aortic wall was assumed rigid. In reality, experimental data on the
492 changes in ascending aortic wall material properties for BAV patients is currently
493 limited. Incorporating a non-rigid wall would introduce a range of variables for which
494 data is lacking; this would limit cross-BAV comparisons. In addition, previous studies
495 have showed that the aortic wall in BAV patients presents with excessive stiffness and
496 reduced compliance in comparison with patients with a TAV [71-73]. Hence, for these
497 patients, it is preferable to assume the effect of wall motion in velocity and WSS fields
498 as negligible [81]. Moreover, previous computational studies have noted that the
499 essential characteristics of blood flow can be detected with the use of rigid wall models,
500 for vessels such as the aorta [82]. Future studies assessing moving aortic walls would be
501 beneficial, but characterisation of their mechanical properties needs to be evidence based
502 and need to be specific to BAV phenotype.

503 Despite being anisotropic, valve tissue was assumed to follow linear, elastic and
504 isotropic mechanical properties. Nonetheless, previous studies show that the
505 physiological strain of aortic valve leaflets have a cyclical stretch of 10% [36-38]. In
506 addition, the nonlinear stress-strain curve of the cardiac tissue can be approximated by
507 two linear regions, where one occurs at low strain range (below 15%) and another
508 happens at high strain rates [83]. At low strain rates, such linearity increases; therefore,
509 given the reported range of cardiac tissue deformation in the aortic valve relevant to the
510 simulations in our study, this assumption does not appear unjustifiable, and is consistent
511 with previous studies [9, 15, 22, 39, 40]. Additionally, there is an inherent limitation in
512 assigning anisotropic, and hyper-elastic material properties to cusps of BAVs in that
513 characterisation of material properties of BAV cusps are not readily available in
514 literature, and certainly not stratified according to phenotype.

515 The model used in this study employed an idealised pressure waveform (rather than
516 patient specific [13, 84]) and no coupling with a lumped-parameter model for branching
517 arteries was incorporated. However, there are challenges with tuning of the parameter
518 values of a lumped parameter heart model [85]. Moreover, the aim of this proof-of-

519 concept study was the cross-comparison between TAV and BAV models which did not
520 require a lumped-parameter model coupling. This aspect can be overcome in future
521 studies; nonetheless, our model predictions are consistent with the clinical and
522 experimental literature available. This is likely because primary flow through the
523 ascending aorta is mostly undisturbed by excluding branching arteries.

524 **6. Conclusion**

525 BAV related haemodynamics and mechanics are altered in comparison with a TAV and
526 different phenotypes yield different characteristics: type 0 BAV yields the least
527 haemodynamic and mechanical impact, but its orifice orientation generates different
528 magnitude and distribution of valve stress; type 1 BAVs present with similar quantitative
529 haemodynamic and mechanical features across subtypes. Moreover, for the first time, a
530 type 2 BAV was simulated computationally and our results suggest that this phenotype
531 may be associated with greater valve and aortic damage in comparison with the other
532 categories. These differences between and within categories of BAV may be central to
533 subsequent pathology, including the location of such pathology. Our FSI model can
534 therefore aid clinicians in patient risk stratification, estimating patients at a larger risk to
535 develop complications derived from BAV abnormal haemodynamics and mechanics.
536

537 **Conflicts of interest**

538 The authors declare that they have no competing interests.

539 **Funding details**

540 No relevant funding.

541 **Statement involving human and animal rights**

542 No human or animal studies were carried out by the authors for this article.

References

1. Ward, C., *Clinical significance of the bicuspid aortic valve*. Heart, 2000. **83**(1): p. 81-5.
2. Robicsek, F., et al., *The congenitally bicuspid aortic valve: how does it function? Why does it fail?* Ann Thorac Surg, 2004. **77**(1): p. 177-85.
3. Sievers, H.H. and C. Schmidtke, *A classification system for the bicuspid aortic valve from 304 surgical specimens*. J Thorac Cardiovasc Surg, 2007. **133**(5): p. 1226-33.
4. Mahadevia, R., et al., *Bicuspid aortic cusp fusion morphology alters aortic three-dimensional outflow patterns, wall shear stress, and expression of aortopathy*. Circulation, 2014. **129**(6): p. 673-82.
5. Mirabella, L., et al., *MRI-based Protocol to Characterize the Relationship Between Bicuspid Aortic Valve Morphology and Hemodynamics*. Ann Biomed Eng, 2015. **43**(8): p. 1815-27.
6. Rodriguez-Palomares, J.F., et al., *Aortic flow patterns and wall shear stress maps by 4D-flow cardiovascular magnetic resonance in the assessment of aortic dilatation in bicuspid aortic valve disease*. J Cardiovasc Magn Reson, 2018. **20**(1): p. 28.
7. Sievers, H.H., et al., *Toward individualized management of the ascending aorta in bicuspid aortic valve surgery: the role of valve phenotype in 1362 patients*. J Thorac Cardiovasc Surg, 2014. **148**(5): p. 2072-80.
8. Markl, M., P.J. Kilner, and T. Ebbers, *Comprehensive 4D velocity mapping of the heart and great vessels by cardiovascular magnetic resonance*. J Cardiovasc Magn Reson, 2011. **13**: p. 7.
9. De Hart, J., et al., *A three-dimensional computational analysis of fluid-structure interaction in the aortic valve*. J Biomech, 2003. **36**(1): p. 103-12.
10. De Hart, J., et al., *A two-dimensional fluid-structure interaction model of the aortic valve [correction of value]*. J Biomech, 2000. **33**(9): p. 1079-88.
11. Spuhler, J.H., et al., *3D Fluid-Structure Interaction Simulation of Aortic Valves Using a Unified Continuum ALE FEM Model*. Front Physiol, 2018. **9**: p. 363.
12. Chen, Y. and H.X. Luo, *A computational study of the three-dimensional fluid-structure interaction of aortic valve*. Journal of Fluids and Structures, 2018. **80**: p. 332-349.
13. Bahraseman, H.G., et al., *Effect of exercise on blood flow through the aortic valve: a combined clinical and numerical study*. Computer Methods in Biomechanics and Biomedical Engineering, 2014. **17**(16): p. 1821-1834.
14. Bahraseman, H.G., et al., *Estimation of maximum intraventricular pressure: a three-dimensional fluid-structure interaction model*. Biomed Eng Online, 2013. **12**: p. 122.
15. Kuan, M.Y. and D.M. Espino, *Systolic fluid-structure interaction model of the congenitally bicuspid aortic valve: assessment of modelling requirements*. Comput Methods Biomech Biomed Engin, 2015. **18**(12): p. 1305-20.
16. Cao, K., et al., *Simulations of morphotype-dependent hemodynamics in non-dilated bicuspid aortic valve aortas*. J Biomech, 2017. **50**: p. 63-70.
17. Liu, J., J.A. Shar, and P. Sucusky, *Wall Shear Stress Directional Abnormalities in BAV Aortas: Toward a New Hemodynamic Predictor of Aortopathy?* Front Physiol, 2018. **9**: p. 993.

18. Kimura, N., et al., *Patient-specific assessment of hemodynamics by computational fluid dynamics in patients with bicuspid aortopathy*. J Thorac Cardiovasc Surg, 2017. **153**(4): p. S52-S62 e3.
19. Marom, G., et al., *Effect of asymmetry on hemodynamics in fluid-structure interaction model of congenital bicuspid aortic valves*. Conf Proc IEEE Eng Med Biol Soc, 2012. **2012**: p. 637-40.
20. Lavon, K., et al., *Fluid-Structure Interaction Models of Bicuspid Aortic Valves: The Effects of Nonfused Cusp Angles*. J Biomech Eng, 2018. **140**(3).
21. Hager, A., et al., *Diameters of the thoracic aorta throughout life as measured with helical computed tomography*. J Thorac Cardiovasc Surg, 2002. **123**(6): p. 1060-6.
22. Mohammadi, H., R. Cartier, and R. Mongrain, *The impact of the aortic valve impairment on the distant coronary arteries hemodynamics: a fluid-structure interaction study*. Med Biol Eng Comput, 2017. **55**(10): p. 1859-1872.
23. Mei, S., et al., *Hemodynamics through the congenitally bicuspid aortic valve: a computational fluid dynamics comparison of opening orifice area and leaflet orientation*. Perfusion, 2016.
24. Piatti, F., et al., *4D Flow Analysis of BAV-Related Fluid-Dynamic Alterations: Evidences of Wall Shear Stress Alterations in Absence of Clinically-Relevant Aortic Anatomical Remodeling*. Front Physiol, 2017. **8**: p. 441.
25. Oliveira, D., et al., *Bicuspid aortic valve aortopathies: An hemodynamics characterization in dilated aortas*. Comput Methods Biomech Biomed Engin, 2019. **22**(8): p. 815-826.
26. Halevi, R., et al., *Fluid-structure interaction modeling of calcific aortic valve disease using patient-specific three-dimensional calcification scans*. Med Biol Eng Comput, 2016. **54**(11): p. 1683-1694.
27. Bonow, R.O., et al., *ACC/AHA 2006 guidelines for the management of patients with valvular heart disease: a report of the American College of Cardiology/American Heart Association Task Force on Practice Guidelines*. J Am Coll Cardiol, 2006. **48**(3): p. e1-148.
28. Nishimura, R.A., et al., *2014 AHA/ACC guideline for the management of patients with valvular heart disease: a report of the American College of Cardiology/American Heart Association Task Force on Practice Guidelines*. J Am Coll Cardiol, 2014. **63**(22): p. e57-185.
29. van Loon, R., et al., *Comparison of various fluid-structure interaction methods for deformable bodies*. Computers & Structures, 2007. **85**(11-14): p. 833-843.
30. Shewchuk, J.R. *What is a Good Linear Element? Interpolation, Conditioning, and Quality Measures*. in *Eleventh International Meshing Roundtable*. 2002.
31. Belytschko, T., J.I. Lin, and C.S. Tsay, *Explicit Algorithms for the Nonlinear Dynamics of Shells*. Computer Methods in Applied Mechanics and Engineering, 1984. **42**(2): p. 225-251.
32. Hallquist, J., *LS-DYNA Keyword User's Manual*. 2006, Livermore Software Technology Corporation: LSTC, USA.
33. Carty, G., S. Chatpun, and D.M. Espino, *Modeling Blood Flow Through Intracranial Aneurysms: A Comparison of Newtonian and Non-Newtonian Viscosity*. Journal of Medical and Biological Engineering, 2016. **36**(3): p. 396-409.
34. Heuzé, O., *General form of the Mie-Grüneisen equation of state*. Comptes Rendus Mecanique, 2012. **340**: p. 679-687.

35. Wang, S.H., L.P. Lee, and J.S. Lee, *A linear relation between the compressibility and density of blood*. J Acoust Soc Am, 2001. **109**(1): p. 390-6.
36. El-Hamamsy, I., A.H. Chester, and M.H. Yacoub, *Cellular regulation of the structure and function of aortic valves*. J Adv Res, 2010. **1**: p. 5–12.
37. Ferdous, Z., H. Jo, and R.M. Nerem, *Strain magnitude-dependent calcific marker expression in valvular and vascular cells*. Cells Tissues Organs, 2013. **197**(5): p. 372-83.
38. Metzler, S.A., et al., *Cyclic strain regulates pro-inflammatory protein expression in porcine aortic valve endothelial cells*. J Heart Valve Dis, 2008. **17**(5): p. 571-7; discussion 578.
39. Luraghi, G., et al., *Does clinical data quality affect fluid-structure interaction simulations of patient-specific stenotic aortic valve models?* J Biomech, 2019. **94**: p. 202-210.
40. Wu, W., et al., *Fluid-Structure Interaction Model of a Percutaneous Aortic Valve: Comparison with an In Vitro Test and Feasibility Study in a Patient-Specific Case*. Ann Biomed Eng, 2016. **44**(2): p. 590-603.
41. Sturla, F., et al., *Impact of modeling fluid-structure interaction in the computational analysis of aortic root biomechanics*. Med Eng Phys, 2013. **35**(12): p. 1721-30.
42. Espino, D.M., D.E. Shepherd, and D.W. Hukins, *Evaluation of a transient, simultaneous, arbitrary Lagrange-Euler based multi-physics method for simulating the mitral heart valve*. Comput Methods Biomech Biomed Engin, 2014. **17**(4): p. 450-8.
43. Espino, D.M., D.E.T. Shepherd, and D.W.L. Hukins, *Transient large strain contact modelling: A comparison of contact techniques for simultaneous fluid-structure interaction*. European Journal of Mechanics B-Fluids, 2015. **51**: p. 54-60.
44. Barker, A.J., C. Lanning, and R. Shandas, *Quantification of hemodynamic wall shear stress in patients with bicuspid aortic valve using phase-contrast MRI*. Ann Biomed Eng, 2010. **38**(3): p. 788-800.
45. Barker, A.J., et al., *Bicuspid aortic valve is associated with altered wall shear stress in the ascending aorta*. Circ Cardiovasc Imaging, 2012. **5**(4): p. 457-66.
46. Bonomi, D., et al., *Influence of the aortic valve leaflets on the fluid-dynamics in aorta in presence of a normally functioning bicuspid valve*. Biomech Model Mechanobiol, 2015. **14**(6): p. 1349-61.
47. Dasi, L.P., et al., *Fluid mechanics of artificial heart valves*. Clin Exp Pharmacol Physiol, 2009. **36**(2): p. 225-37.
48. Bock, J., et al., *In vivo noninvasive 4D pressure difference mapping in the human aorta: phantom comparison and application in healthy volunteers and patients*. Magn Reson Med, 2011. **66**(4): p. 1079-88.
49. McNally, A., A. Madan, and P. Sucusky, *Morphotype-Dependent Flow Characteristics in Bicuspid Aortic Valve Ascending Aortas: A Benchtop Particle Image Velocimetry Study*. Front Physiol, 2017. **8**: p. 44.
50. Saikrishnan, N., et al., *In vitro characterization of bicuspid aortic valve hemodynamics using particle image velocimetry*. Ann Biomed Eng, 2012. **40**(8): p. 1760-75.
51. Becker, W., et al., *Bayesian sensitivity analysis of a model of the aortic valve*. J Biomech, 2011. **44**(8): p. 1499-506.

52. Lorenz, R., et al., *4D flow magnetic resonance imaging in bicuspid aortic valve disease demonstrates altered distribution of aortic blood flow helicity*. Magn Reson Med, 2014. **71**(4): p. 1542-53.
53. Burken, J., *Determining the effect of congenital bicuspid aortic valves on aortic dissection using computational fluid dynamics*, in *Biomedical Engineering*. 2012, The University of Iowa.
54. Chandra, S., N.M. Rajamannan, and P. Sucusky, *Computational assessment of bicuspid aortic valve wall-shear stress: implications for calcific aortic valve disease*. Biomech Model Mechanobiol, 2012. **11**(7): p. 1085-96.
55. Cao, K. and P. Sucusky, *Computational comparison of regional stress and deformation characteristics in tricuspid and bicuspid aortic valve leaflets*. Int J Numer Method Biomed Eng, 2017. **33**(3).
56. Gilmanov, A. and F. Sotiropoulos, *Comparative hemodynamics in an aorta with bicuspid and trileaflet valves*. Theoretical and Computational Fluid Dynamics, 2016. **30**(1-2): p. 67-85.
57. Kouhi, E. and Y.S. Morsi, *A parametric study on mathematical formulation and geometrical construction of a stentless aortic heart valve*. J Artif Organs, 2013. **16**(4): p. 425-42.
58. Richards, K.E., et al., *Influence of structural geometry on the severity of bicuspid aortic stenosis*. Am J Physiol Heart Circ Physiol, 2004. **287**(3): p. H1410-6.
59. Baumgartner, H., et al., *Echocardiographic assessment of valve stenosis: EAE/ASE recommendations for clinical practice*. Eur J Echocardiogr, 2009. **10**(1): p. 1-25.
60. Grimard, B.H. and J.M. Larson, *Aortic stenosis: diagnosis and treatment*. Am Fam Physician, 2008. **78**(6): p. 717-24.
61. Akins, C.W., B. Travis, and A.P. Yoganathan, *Energy loss for evaluating heart valve performance*. J Thorac Cardiovasc Surg, 2008. **136**(4): p. 820-33.
62. Manning, W.J., *Asymptomatic aortic stenosis in the elderly: a clinical review*. JAMA, 2013. **310**(14): p. 1490-7.
63. Butcher, J.T. and R.M. Nerem, *Valvular endothelial cells and the mechanoregulation of valvular pathology*. Philos Trans R Soc Lond B Biol Sci, 2007. **362**(1484): p. 1445-57.
64. Hamatani, Y., et al., *Pathological Investigation of Congenital Bicuspid Aortic Valve Stenosis, Compared with Atherosclerotic Tricuspid Aortic Valve Stenosis and Congenital Bicuspid Aortic Valve Regurgitation*. PLoS One, 2016. **11**(8): p. e0160208.
65. Conti, C.A., et al., *Biomechanical implications of the congenital bicuspid aortic valve: a finite element study of aortic root function from in vivo data*. J Thorac Cardiovasc Surg, 2010. **140**(4): p. 890-6, 896 e1-2.
66. Dolan, J.M., et al., *High fluid shear stress and spatial shear stress gradients affect endothelial proliferation, survival, and alignment*. Ann Biomed Eng, 2011. **39**(6): p. 1620-31.
67. Pasta, S., et al., *Difference in hemodynamic and wall stress of ascending thoracic aortic aneurysms with bicuspid and tricuspid aortic valve*. J Biomech, 2013. **46**(10): p. 1729-38.
68. Oliveira, D., et al., *Bicuspid aortic valve aortopathies: An hemodynamics characterization in dilated aortas*. Comput Methods Biomech Biomed Engin, 2019: p. 1-12.

69. Braunwald, E. and R.O. Bonow, *Braunwald's heart disease : a textbook of cardiovascular medicine*. 9th ed. 2012, Philadelphia: Saunders. xxiv, 1961 p.
70. Vergara, C., et al., *Influence of bicuspid valve geometry on ascending aortic fluid dynamics: a parametric study*. *Artif Organs*, 2012. **36**(4): p. 368-78.
71. Rooprai, J., et al., *Thoracic Aortic Aneurysm Growth in Bicuspid Aortic Valve Patients: Role of Aortic Stiffness and Pulsatile Hemodynamics*. *J Am Heart Assoc*, 2019. **8**(8): p. e010885.
72. Goudot, G., et al., *Aortic Wall Elastic Properties in Case of Bicuspid Aortic Valve*. *Front Physiol*, 2019. **10**: p. 299.
73. Nistri, S., et al., *Aortic elasticity and size in bicuspid aortic valve syndrome*. *Eur Heart J*, 2008. **29**(4): p. 472-9.
74. Poullis, M.P., et al., *Ascending aortic curvature as an independent risk factor for type A dissection, and ascending aortic aneurysm formation: a mathematical model*. *European Journal of Cardio-Thoracic Surgery*, 2008. **33**(6): p. 995–1001.
75. Gode, S., et al., *The role of the angle of the ascending aortic curvature on the development of type A aortic dissection: ascending aortic angulation and dissection*. *Interact Cardiovasc Thorac Surg*, 2019. **29**(4): p. 615-620.
76. Doorly, D. and S. Sherwin, *Geometry and flow*, in *Cardiovascular Mathematics: Modeling and simulation of the circulatory system*, L. Formaggia, A. Quarteroni, and A. Veneziani, Editors. 2009, Springer.
77. Faggiano, E., et al., *Helical flows and asymmetry of blood jet in dilated ascending aorta with normally functioning bicuspid valve*. *Biomech Model Mechanobiol*, 2013. **12**(4): p. 801-13.
78. Viscardi, F., et al., *Comparative finite element model analysis of ascending aortic flow in bicuspid and tricuspid aortic valve*. *Artif Organs*, 2010. **34**(12): p. 1114-20.
79. Cao, K. and P. Sucusky, *Effect of Bicuspid Aortic Valve Cusp Fusion on Aorta Wall Shear Stress: Preliminary Computational Assessment and Implication for Aortic Dilatation*. *World J of Cardiovasc Dis*, 2015. **05**(06): p. 129-140.
80. Algabri, Y.A., et al., *Computational study on hemodynamic changes in patient-specific proximal neck angulation of abdominal aortic aneurysm with time-varying velocity*. *Australas Phys Eng Sci Med*, 2019. **42**(1): p. 181-190.
81. Simão, M., et al., *Aorta Ascending Aneurysm Analysis Using CFD Models towards Possible Anomalies*. *Fluids* 2017, 2(2), 31, 2017. **2**(31).
82. Formaggia, L., K. Perktold, and A. Quarteroni, *Basic mathematical models and motivations*, in *Cardiovascular Mathematics: Modeling and simulation of the circulatory system*, L. Formaggia, A. Quarteroni, and A. Veneziani, Editors. 2009, Springer.
83. Choudhury, N., et al., *Local mechanical and structural properties of healthy and diseased human ascending aorta tissue*. *Cardiovasc Pathol*, 2009. **18**(2): p. 83-91.
84. Bahraseman, H., et al., *Combining numerical and clinical methods to assess aortic valve hemodynamics during exercise*. *Perfusion*, 2014. **29**(4): p. 340-350.
85. Kim, H.J., et al., *On coupling a lumped parameter heart model and a three-dimensional finite element aorta model*. *Ann Biomed Eng*, 2009. **37**(11): p. 2153-69.
86. Alastruey, J., et al., *On the impact of modelling assumptions in multi-scale, subject-specific models of aortic haemodynamics*. *J R Soc Interface*, 2016. **13**(119).

87. Yap, C.H., N. Saikrishnan, and A.P. Yoganathan, *Experimental measurement of dynamic fluid shear stress on the ventricular surface of the aortic valve leaflet*. *Biomech Model Mechanobiol*, 2012. **11**(1-2): p. 231-44.
88. Chandran, K.B., S.E. Rittgers, and A.P. Yoganathan, *Biofluid mechanics : the human circulation*. 2007, Boca Raton: CRC/Taylor & Francis. 419 p.

Supplementary material

Fig. S1 Peak systolic velocity contours [m/s] at multiple horizontal section cuts (isometric view) for TAV, BAV type 0 anterior-posterior (AP), type 0 lateral, type 1 N-L, type 1 N-R, type 1 R-L, and type 2. Different velocity scales are used for the models, to better highlight secondary aortic flow patterns in each case.

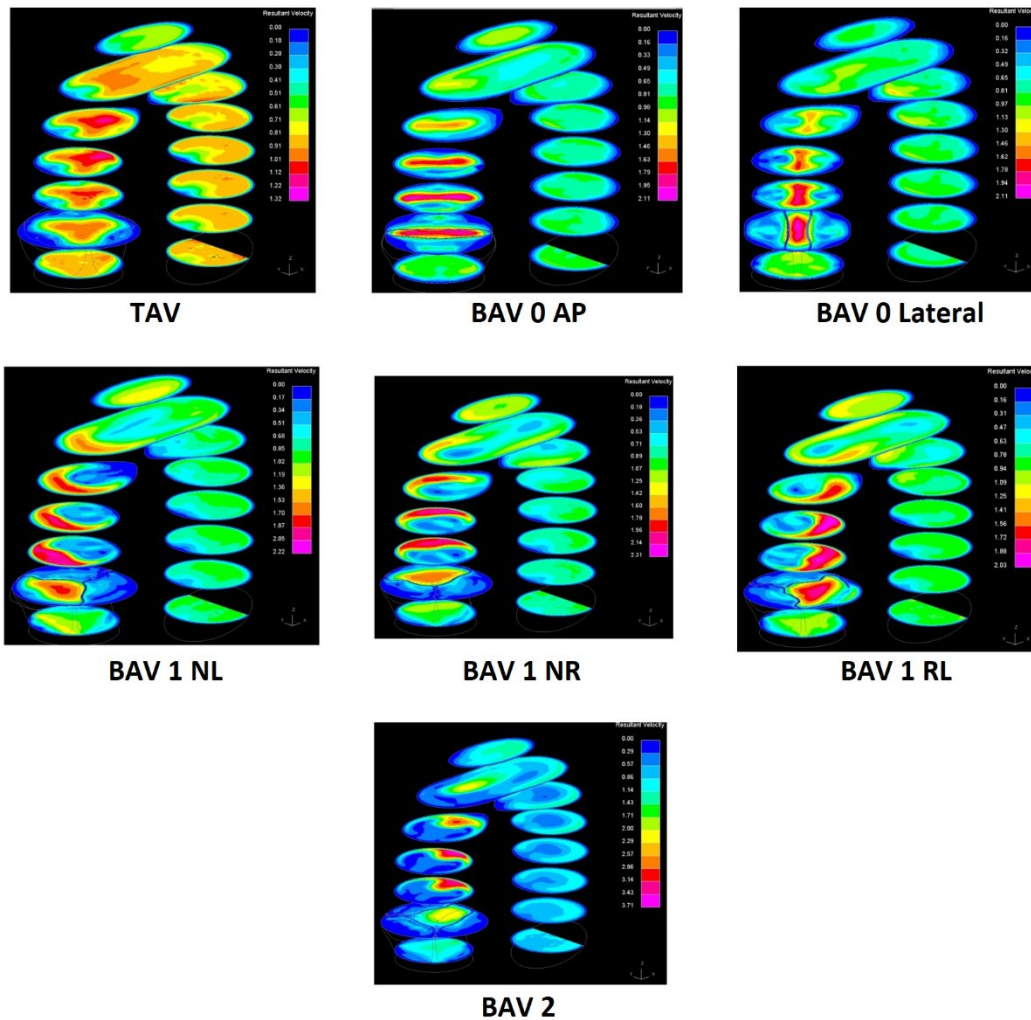


Fig. S2 Time-averaged WSS (TAWSS) at the B-B section for all models (full cardiac cycle).

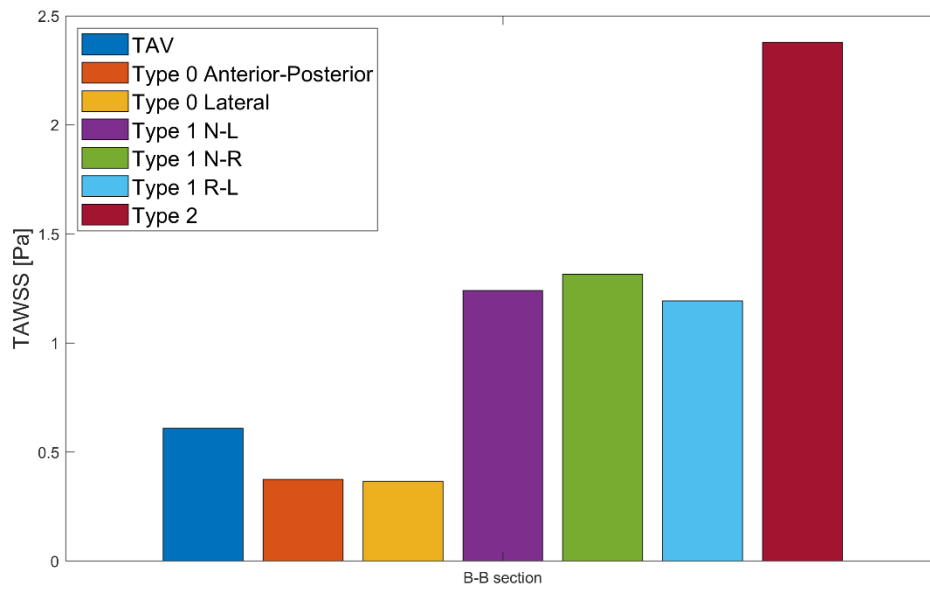
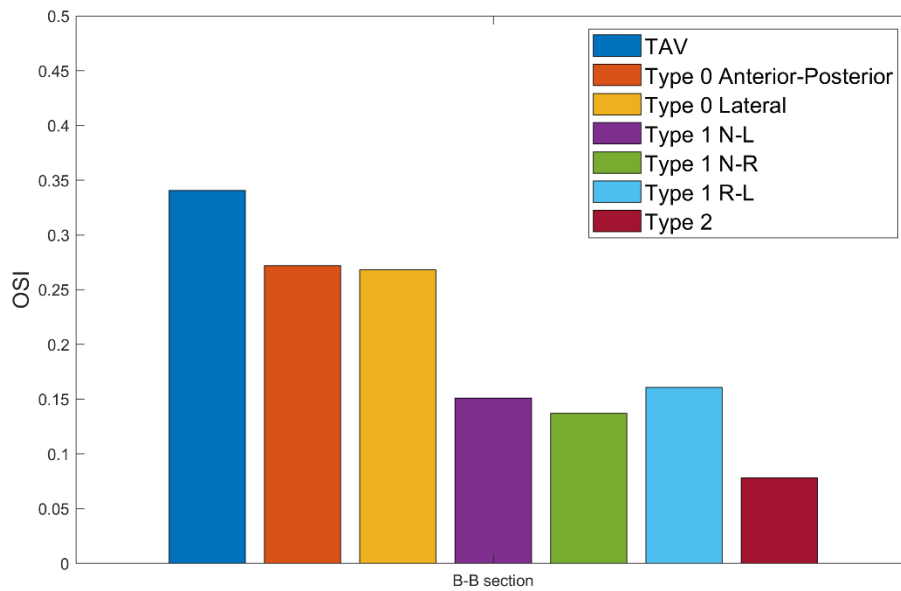


Fig. S3 Oscillatory shear index (OSI) at the B-B section for all models (full cardiac cycle).



Figures and tables for review (in order of citation on the text)

Table 1 Dimensions of BAV models (also see Fig. 2 and Fig. 3)

	TAV	BAV			
		Type 0 Anterior-Posterior	Type 0 Lateral	Type 1 N-L; N-R; R-L	Type 2
Sinus number	3	2	2	3	3
R_a (mm)	12.5	12.5	12.5	12.5	12.5
A_n (°)	118	180	180	138	138
A_l/A_r (°)	118	180	180	109	109
L_v (mm)	16.7	17.5	17.5	16.7	16.7
H_v (mm)	10.5	10.5	10.5	10.5	10.5
D_s (mm)	6	6	6	6	6
H_s (mm)	21	21	21	21	21

Notes: R_a , aortic radius; A_n , non-coronary cusp angle; A_l , left cusp angle; A_r , right cusp angle; L_v , non-coronary cusp arc length; H_v , cusp height; D_s , sinus depth; H_s , sinus height.

Fig. 1 BAV geometries. a) Type 0 anterior-posterior, b) type 0 lateral, c) type 1 N-L, d) type 1 N-R, e) type 1 R-L, f) type 2. Note: the raphe is highlighted with a black line

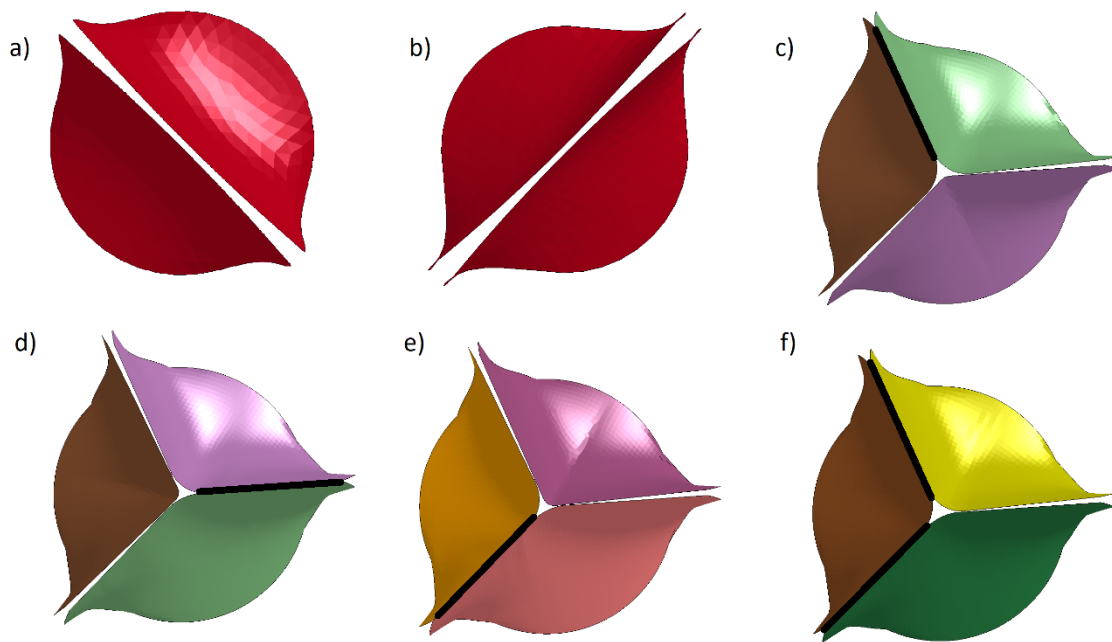


Fig. 2 Model dimensions, with a) view of the TAV leaflets and b) sagittal view of the model, including aortic root and ascending aorta. Notes: R_a , aortic radius; A_n , non-coronary cusp angle; A_l , left cusp angle; L_v , non-coronary cusp arc length; H_v , cusp height; D_s , sinus depth; H_s , sinus height

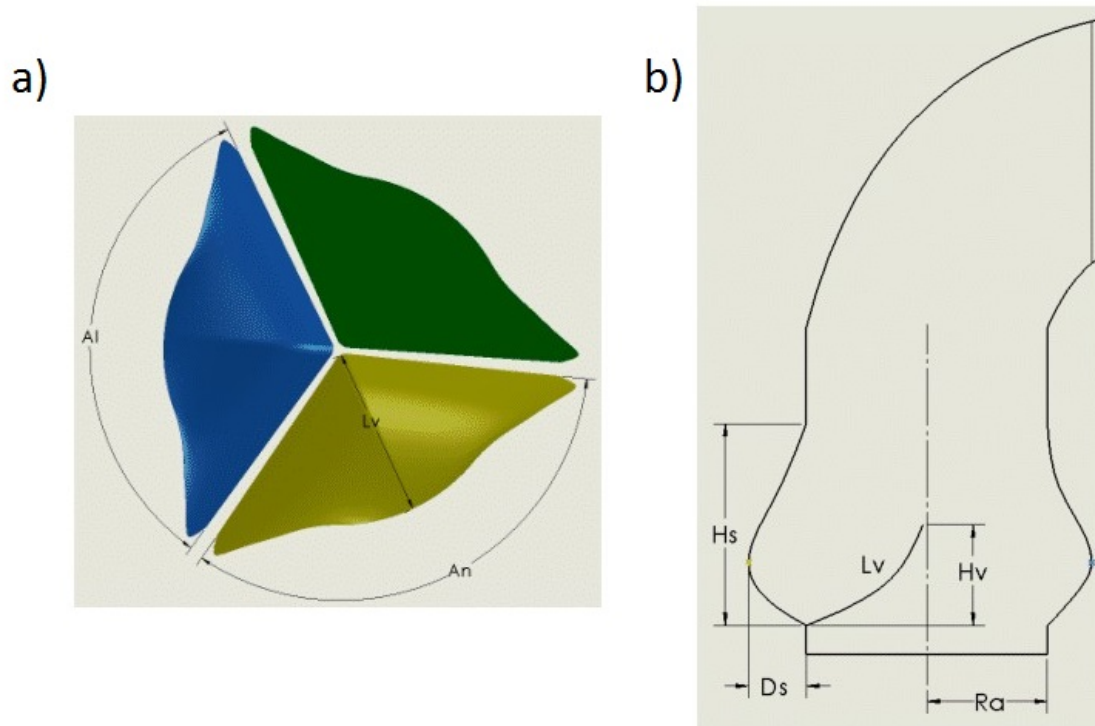


Fig. 3 Full aortic geometry, including a) mesh view of a complete aortic model with a TAV, b) coronal view with A-A cross-section, c) sagittal view, with B-B, C-C and D-D cross-sections. Note: Blue, green and yellow dots represent inlet, outlet and fixed constraint boundary conditions, respectively

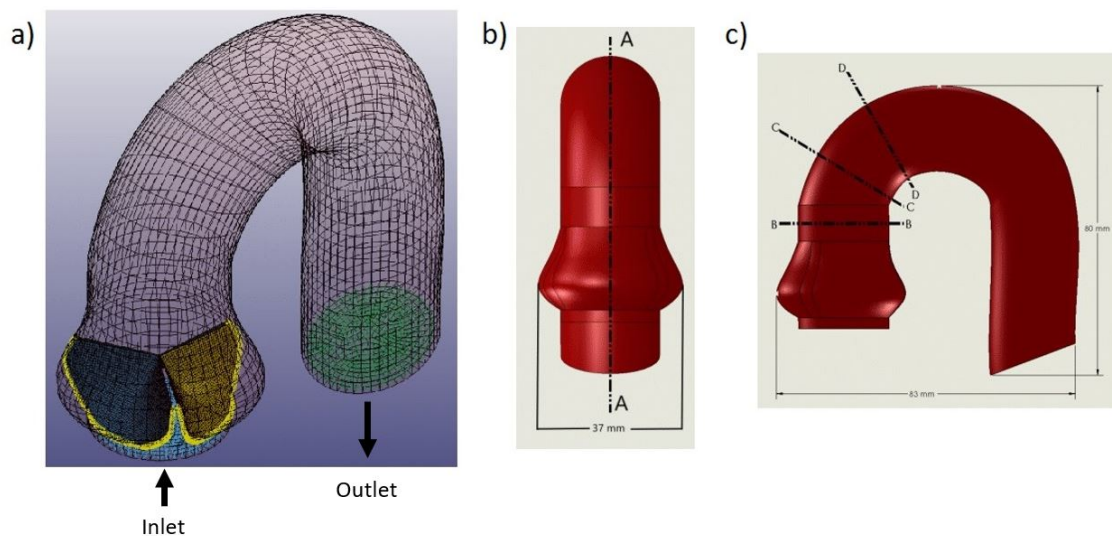


Fig. 4 Time-dependent boundary conditions imposed at the inlet (adapted from [78]) and outlet (adapted from [86]) boundaries

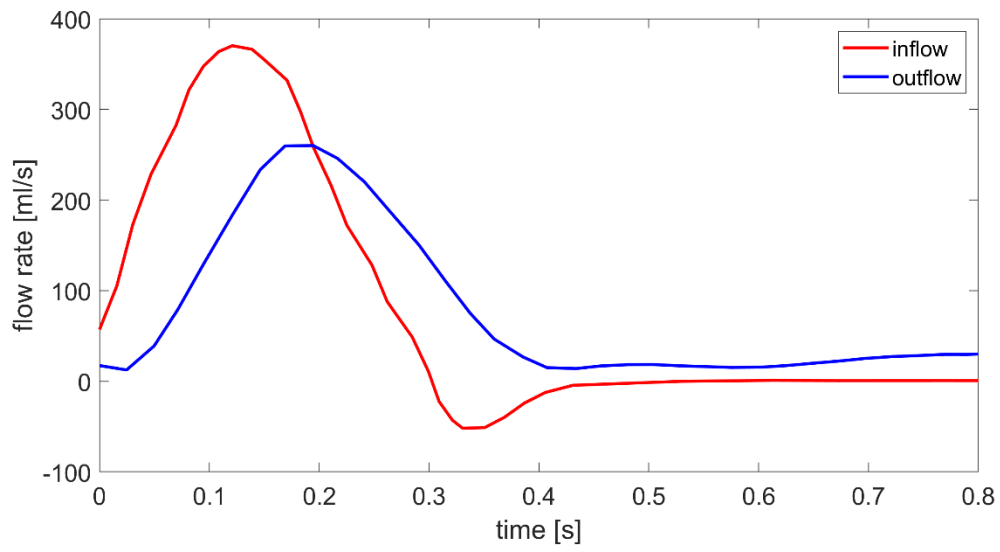


Fig. 5 Peak systolic velocity contours [m/s] at multiple horizontal section cuts (isometric view) for TAV, BAV type 0 anterior-posterior (AP), type 0 lateral, type 1 N-L, type 1 N-R, type 1 R-L, and type 2

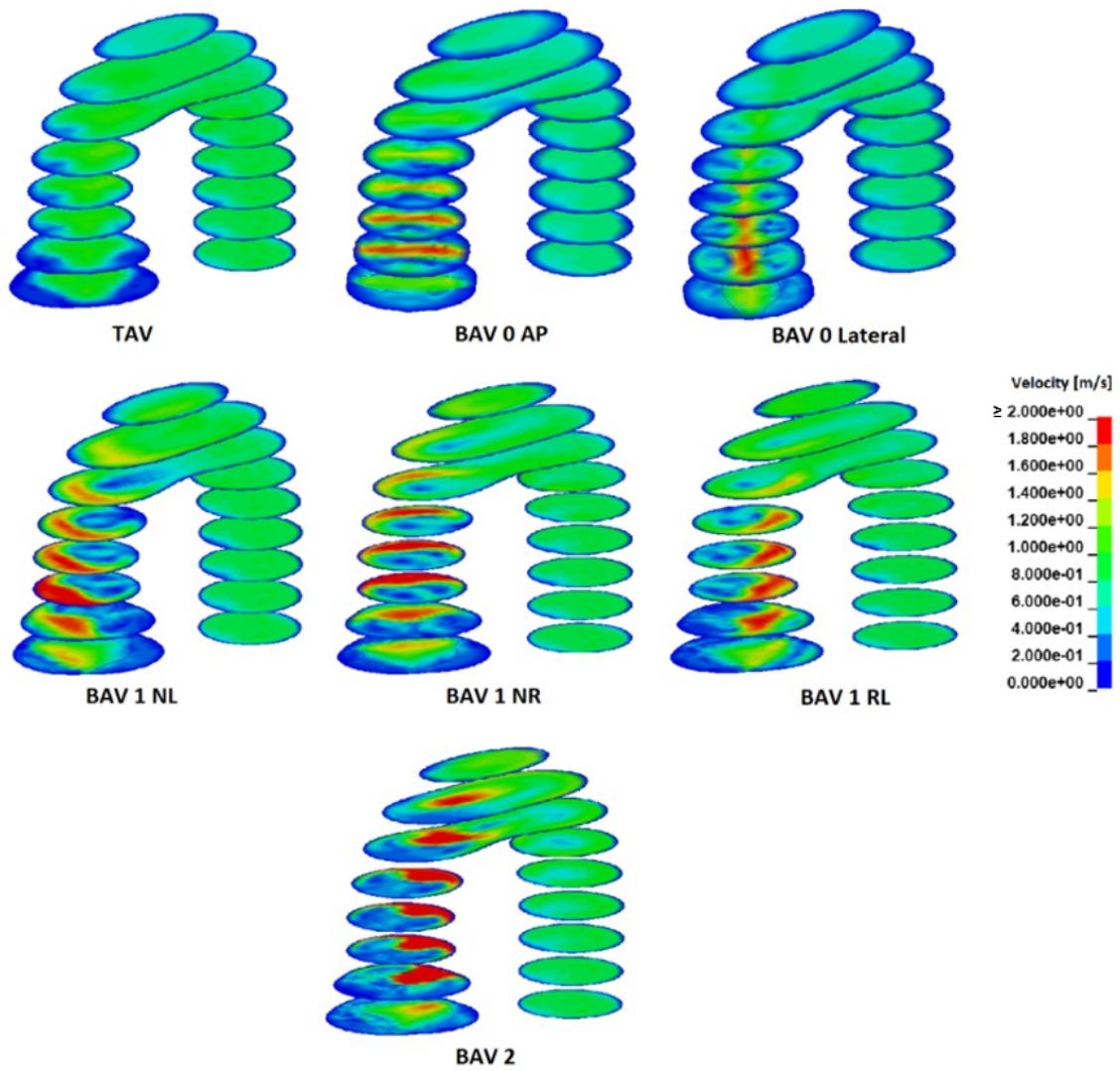


Table 2 Haemodynamic predictions from our computational model and literature results

	Prediction	TAV	BAV					
			Type 0 Anterior-Posterior	Type 0 Lateral	Type 1 N-L	Type 1 N-R	Type 1 R-L	Type 2
Peak velocity [m/s]	Our study	1.52	2.3	2.2	2.38	2.47	2.4	3.7
	<i>In vivo</i> [4-6]	0.9 – 1.8	-	-	-	-	2 – 3	-
	<i>In vitro</i> [49, 50, 87]	1.5 – 2.3	-	-	3.9	-	2.9 - 3.1	-
	<i>In silico</i> (CFD and FSI) [9, 15, 16, 23]	1.3 – 2.3	0.76 – 3.17	3.21	1.85	1.73	1.75	-
ΔP [mmHg]	Our study	4.5	15	15	13.1	14.3	15	37
	<i>In vivo</i> [48, 88]	< 10	-	-	-	-	-	-
	<i>In vitro</i> [50]	17.2	-	-	-	-	-	-
	<i>In silico</i> (CFD) [23]	5	22	22	-	-	-	-
FRR [%]	Our study	0	4.4	3.5	10.1	10.8	9.8	13.3
	<i>In vivo</i> [44]	0.3 – 0.9	-	-	-	-	-	-
	<i>In silico</i> (CFD) [46]	0	11.18	-	-	-	-	-
GOA [cm ²]	Our study	4.13	2	2.34	3.65	3.54	2.84	1.65
EOA [cm ²]	Our study	3.38	1.85	1.85	1.98	1.90	1.85	1.18
	Clinical guidelines [59-61]	Normal	Mild stenosis	Mild stenosis	Mild stenosis	Mild stenosis	Mild stenosis	Moderate stenosis

Fig. 6 Velocity vectors (m/s) at B-B section plane (top view) to show helix flow for TAV, BAV type 0 Anterior-Posterior, type 0 Lateral, type 1 N-L, type 1 N-R, type 1 R-L, and type 2. Note: BAV type 0 vectors are scaled in size, to be visible

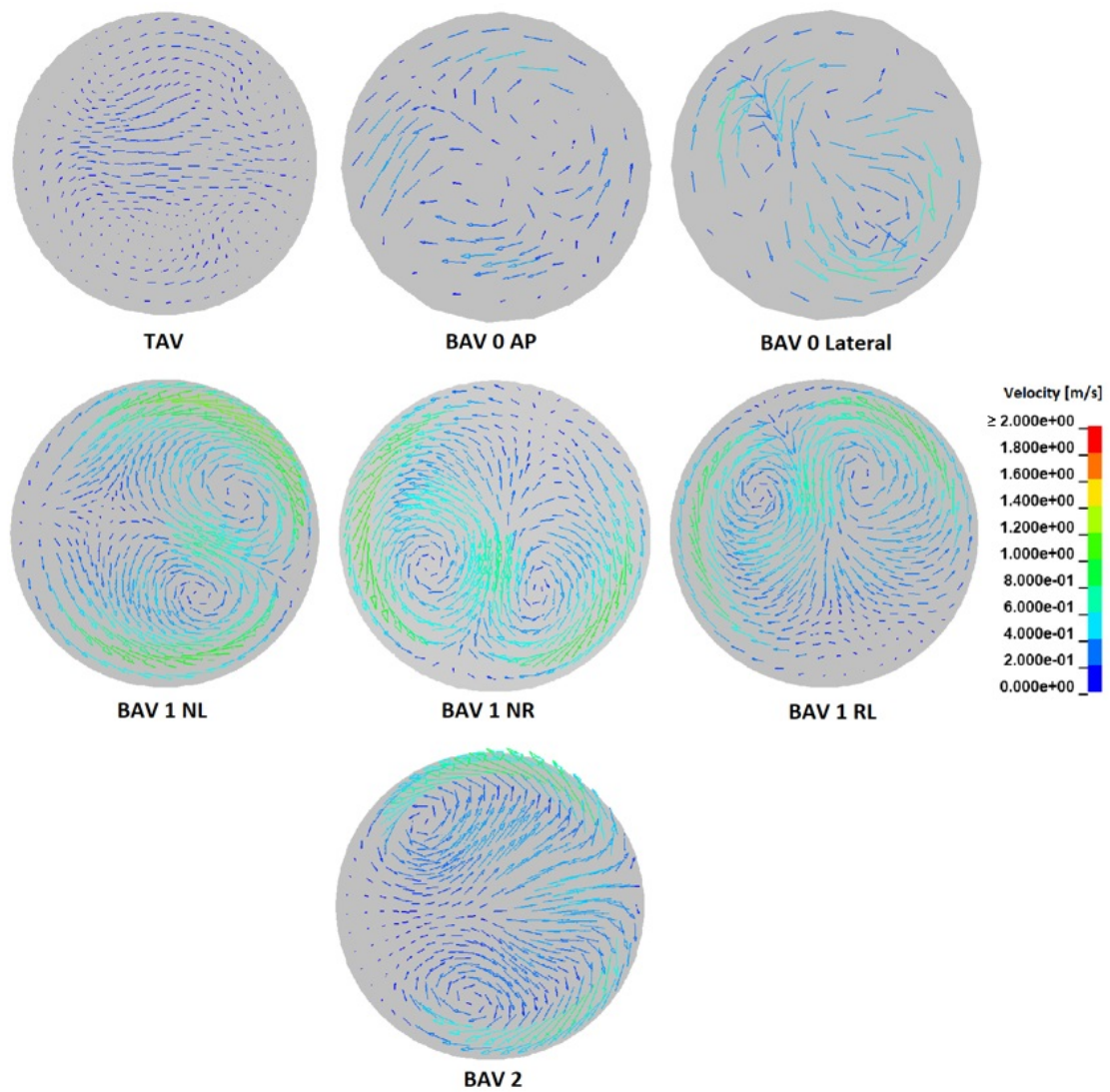


Table 3 Peak systolic stress predictions from our computational model and literature results

	Prediction	TAV	BAV					
			Type 0 Anterior-Posterior	Type 0 Lateral	Type 1 N-L	Type 1 N-R	Type 1 R-L	Type 2
WSS [Pa]	Our study	1.3	0.8	0.78	2.65	2.81	2.55	5.08
	<i>In vivo</i> [6, 45]	0.43 - 3	-	-	-	-	0.67 - 1	-
	<i>In silico</i> (CFD and FSI) [16, 17]	0.75 – 5			2.65	2.45	2.8	-
Von Mises stress [kPa]	Our study	300	270	600	590	630	610	1610
	<i>In silico</i> (CFD and FSI) [51, 57]	160 – 343	280		-	-	-	-

Fig. 7 Peak systolic WSS magnitude [Pa] at all cross-sections

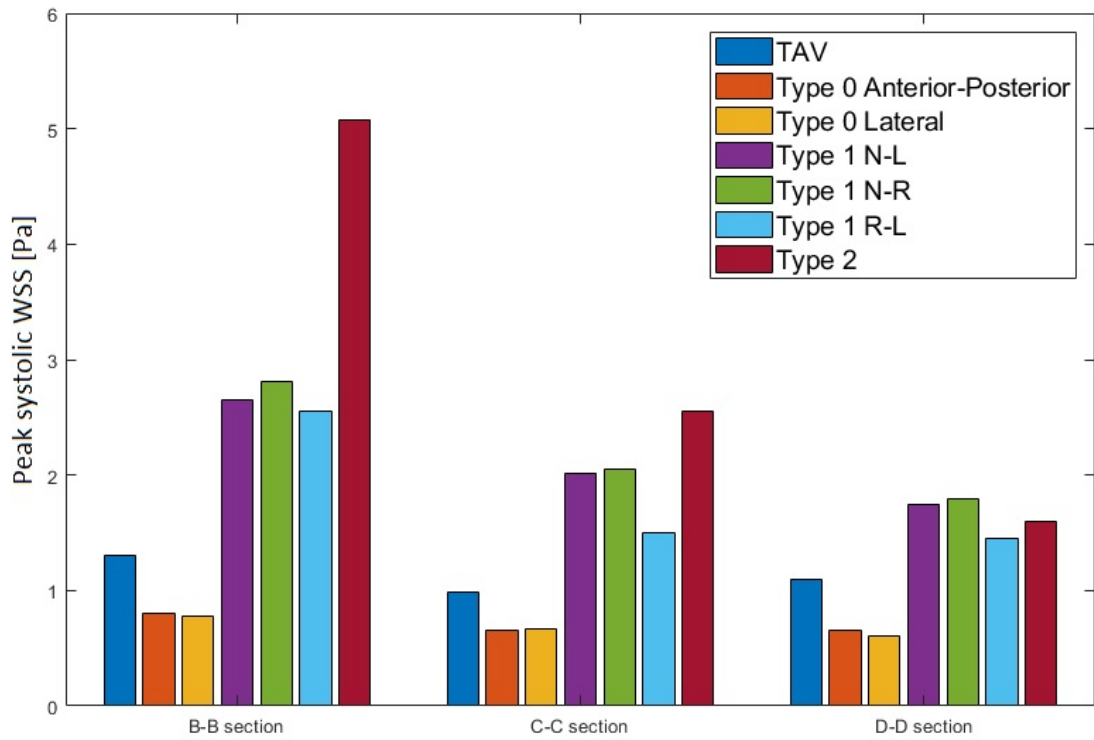


Fig. 8 Valve area-averaged Von Mises stress through the systolic phase

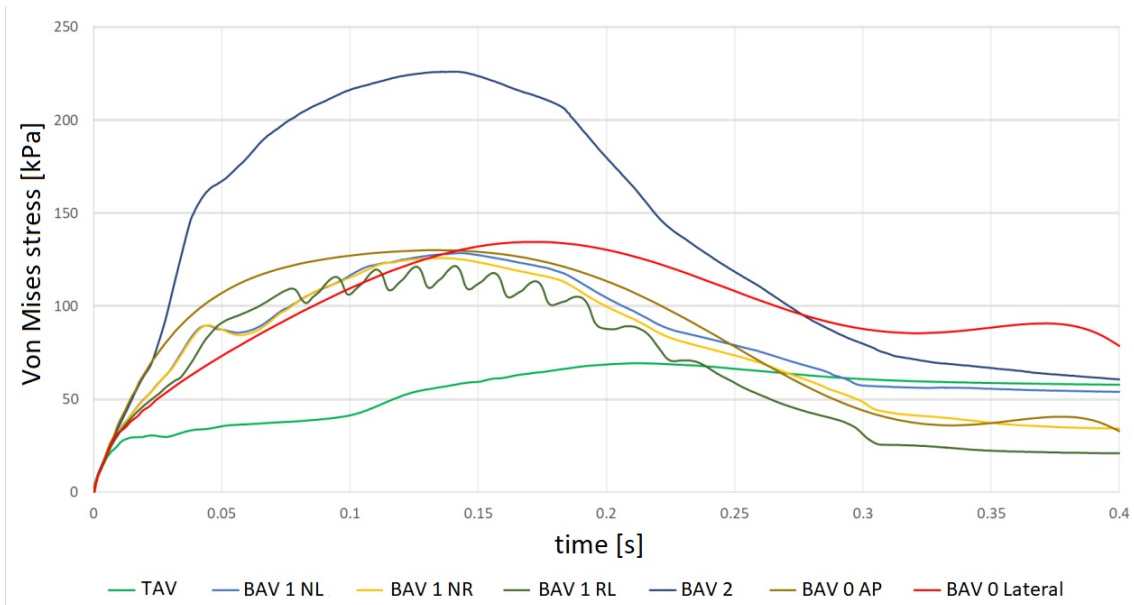


Fig. 9 Von Mises (Pa) stress contours at peak systole for TAV, BAV type 0 Anterior-Posterior, type 0 Lateral, type 1 N-L, type 1 N-R, type 1 R-L, and type 2

